MODELING CONACT LINE DYNAMICS IN EVAPORATING MENISCI

Joel L.Plawsky*, Arya Chatterjee and Peter C. Wayner, Jr.
Department of Chemical and Biological Engineering,
Rensselaer Polytechnic Institute, Troy, NY-12180
*plawsky@rpi.edu

ABSTRACT

The Constrained Vapor Bubble is a fundamental fluid mechanics experiment that is scheduled to run aboard the International Space Station starting in August 2009. The experiment is focused on looking at evaporation and condensation processes at the contact line, where vapor, liquid and solid meet. Our goal is to understand how processes that occur on the macroscale affect the transport processes occurring on the microscale.

Since the contact line is a region of film thickness on the order of 100 nm and evaporation and condensation processes are driven by temperature differences only on the order of 10^{-4} K, measurements are difficult and multi-scale modeling is critical to tying in how changes on the macroscale affect what occurs at the contact line. We have developed a model for evaporation/condensation at the contact line. The model solves a nonlinear, fourth-order evolution equation for the film thickness and from that predicts the contact angle, interfacial curvature, fluid flow and evaporation/condensation rate from the meniscus surface. The results of the model can reproduce experimental, ground-based data and we discuss extensions of the model to handle Marangoni convection, hydrodynamic slip and the stability of the meniscus.

Keywords: Heat transfer, contact line, interfacial phenomena

1. INTRODUCTION

Transport processes occurring at the three-phase contact line control much of the behavior we observe in boiling, evaporation, condensation, coating and self assembly processes. Phase change has the potential to address the cooling requirements of future electronic, photonic, and MEMS devices. One can visualize the change-of-phase heat transfer process as a competition between two fundamental resistances. The first is a conduction resistance through a liquid film on a heated surface that is proportional to the thickness of the liquid film. The second resistance is an interfacial resistance that retards liquid molecules from leaving the vapor-liquid interface and is inversely proportional to the cube of the film thickness. A meniscus can be divided into three regions by the interplay between these resistances as shown in Figure 1. In the region where the thinnest film lies (< 50 nm or so), the intermolecular forces are very strong. This leads to a very high resistance for evaporation. In the bulk fluid region (> 300 nm or so) evaporation is retarded due to the large conduction resistance through the liquid film. The overall thermal resistance reaches a minimum in the transition or contact line region (~ 100 nm) where the small film thickness offers limited conduction resistance, the interfacial resistance disappears due to the rapidly increasing film thickness and the curvature of the vapor-liquid interface can promote condensation. An increase in the length of the contact line (due to increase in the extent of the transition region) has been shown to increase the effective heat transfer Horacek et al [1].

The Constrained Vapor Bubble flight experiment is designed to investigate contact line dynamics in the context of a miniature heat pipe operated in microgravity. Prior to launch in August 2009, a series of ground-based experiments were conducted at NASA Glenn Research Center on flight hardware and at Rensselaer on our homemade equipment. This paper will talk a bit about our experiments and our attempts to match a theoretical model to the experimental data collected.

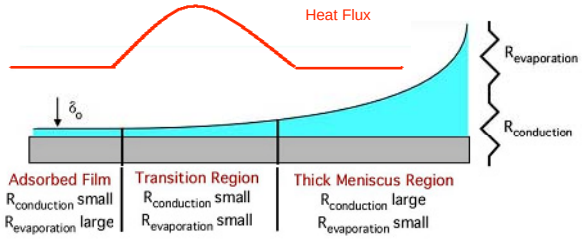

Figure 1 Thermal resistances, film thickness, and heat flux profile within an evaporating meniscus.

2. EXPERIMENTAL APPARATUS & PROCEDURE

The experimental system, shown in Figure 2, is a variant of the constrained vapor bubble (CVB) design used in Zheng et al. [2] and on board the International Space Station. In this situation, a square, glass cuvette of 40×5×5 mm dimensions was fabricated. The cuvette was partially filled with the liquid and then sealed unsing a metal cold finger. The opposite end of the cuvette had an electrical resistance heater attached to it. Menisci formed at the corners of the cuvette and an adsorbed thin film formed on the flat surfaces in contact with the vapor bubble.

The adsorbed film and the corner meniscus were easily viewed through a microscope and the image was recorded for further analysis. Temperature measurements were taken using thermocouples attached to the outer surface of the cuvette. Evaporating menisci were studied using pentane and octane as the working fluid. On Earth, the whole system was studied in a vertical orientation with the heater on the top to insure the menisci in each corner were identical.

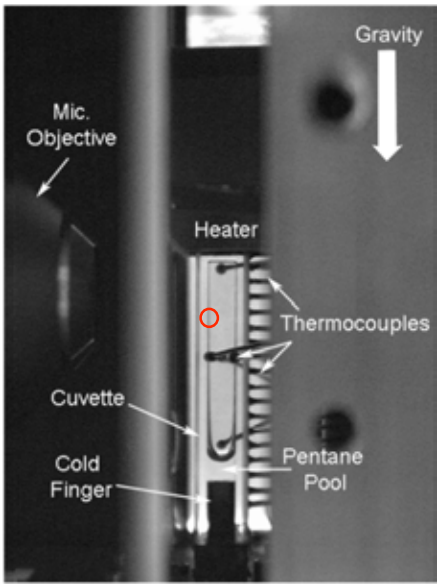

Figure 2 Photograph of the experimental cell with the heater attached to one end and the cooler attached to the other end. The red circle marks the precise location of the sidewall meniscus that is under study.

Meniscus Heat Transfer

A constant heat input was applied to a corner meniscus of pentane/octane to study its evaporative behavior. These fluids were chosen because they perfectly wetted the silica surfaces used. At time, t = 0 the heater power was abruptly increased to a predetermined level and then held steady. As the heat was applied, liquid evaporated from the meniscus and the meniscus receded until a new steady-state was reached where the mass loss due to evaporation was balanced by liquid flow from the bulk of the meniscus driven by capillary forces. Figure 3 shows an interference image of one such meniscus after it had reached steady-state. A number of different heater powers were used ranging from 0.075 – 0.75 W. In addition, experiments were carried out using smooth and roughened surfaces. The rough surfaces were formed either through etching or deposition processes. In all cases the surfaces were silica.

Figures 4 and 5 show experimental film thickness and curvature profiles obtain from an evaporating octane meniscus when the heater input power was set at 0.75W. Two trends are obvious. As the surfaces get rougher, the film thickness profiles spread out and the curvature profile changes significantly. In Figure 5, the curvature profiles exhibit a maximum when the liquid is actively evaporating. As the surfaces get rougher the curvature maximum decreases corresponding to the spreading of the film thickness profile. This maximum exists only when evaporation is occurring and corresponds to the location of the transition region, or the region of minimum thermal resistance. The film thickness there is on the order of 100 nm or less and the temperature differences leading to evaporation are too small to be measured experimentally. Thus we must develop a model that can reproduce the physical features we can measure and use those features to infer how evaporation occurs from the meniscus.

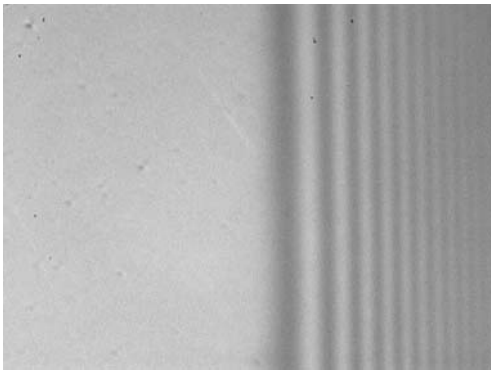

Figure 3 Interference image of an evaporating meniscus

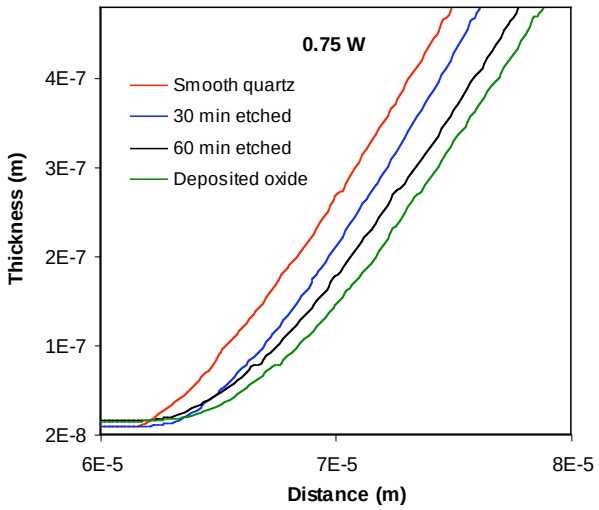

Figure 4 Experimental film thickness profiles for octane on a series of silica surfaces.

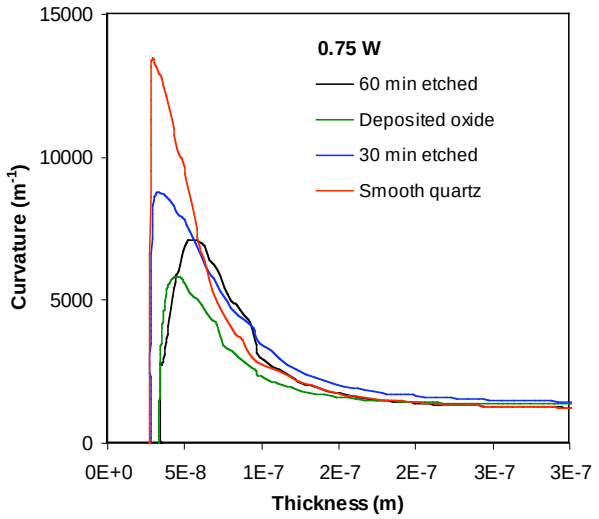

Figure 5 Experimental film curvature profiles on a series of smooth and roughened silica surfaces.

3. MODEL DEVELOPMENT

The modeling of thin, evaporating films begins with the evolution equation developed and studied by Williams and Davis [3], Hwang et &.al [4], Ruckenstein and Jain [5], Sharma and Ruckenstein [6], Burrelbach, Bankhoff, and Davis [7], Reisfeld and Bankhoff [8], and Kheshgi and Scriven [9]. These models were developed primarily for isothermal spreading liquid films on a horizontal surface and have concentrated on describing the critical film thickness at rupture. Evaporation was added to the process later by Burrelback, Bankhoff and Davis [7] who focused again on the stability of the film to rupture and used a constant evaporation rate across the meniscus. Ajaev [10] used a similar equation to simulate the evaporation of a drop. He included the effect of a variable evaporation rate and was able to match the experimental data of Gokhale et al. [11]. A number of other models have been developed for an evaporating meniscus [12-14]. Here we improve upon these models using a variable evaporation rate and incorporating hydrodynamic slip at the solid-liquid interface. We then use the model to try to understand the experimental data we have measured.

The hydrodynamic portion of the model is based on the lubrication approximation. The approximation is assumed to be valid as long as the meniscus thickness is much smaller than its extent and inertial effects are small. Reynolds numbers based on thickness for these films are exceedingly small so dropping the inertial terms is valid. Based on these assumptions, the velocity profile through the film is defined by:

$$\mu_l \frac{\partial^2 u}{\partial y^2} = \frac{dP_l}{dx} \tag{1}$$

Equation (1) is subject to boundary conditions that specify hydrodynamic slip at the liquid-solid interface and Marangoni stress at the vapor-liquid interface.

$$y = 0 \qquad u = \beta_{slip} \frac{du}{dy} \tag{2}$$

$$y = h(x) \qquad \mu \frac{du}{dy} = \frac{d\sigma}{dx} \tag{3}$$

The full velocity profile, *u(y)*, and mass flux, G through the meniscus are now:

$$\begin{aligned} u(y) &= \frac{1}{\mu}\frac{dP_l}{dx}\left(\frac{y^2}{2} - hy\right) + \frac{d\sigma}{dx} y \\ &\quad - \frac{\beta_{slip}}{\mu}\left(h\frac{dP_l}{dy} - \frac{d\sigma}{dx}\right) \end{aligned} \tag{4}$$

$$\begin{aligned} \Gamma = \int_0^{h(x)} \rho_l u \, dy &= \frac{h^3}{3\nu_l}\left(\frac{dP_l}{dx} - \frac{3}{2}\frac{1}{h}\frac{d\sigma}{dx}\right) \\ &\quad + \frac{\beta_{slip}}{\nu_l}\frac{h^3}{h}\left(\frac{dP_l}{dx} - \frac{1}{h}\frac{d\sigma}{dx}\right) \end{aligned} \tag{5}$$

The flow is driven by a pressure force acting along the meniscus. This force arises from three separate phenomena. A capillary force arises due to the curvature gradient of the meniscus. A Marangoni force arises due to the temperature gradient along the meniscus and finally, intermolecular forces between the vapor, liquid, and solid gives rise to a disjoining pressure gradient. This latter force is due to the change in film thickness along the meniscus.

$$\frac{dP_l}{dx} = -\underbrace{\left(\sigma_0 - \gamma\left(T_i - T_v\right)\right)h_{xxx}}_{\text{Capillarity}} + \underbrace{\gamma\frac{dT_i}{dx}h_{xx}}_{\text{Marangoni}} + \underbrace{3\frac{A}{h^4}h_x}_{\text{Disjoining Pressure}} \tag{6}$$

We assume that the change in mass flux through the meniscus is due to evaporation of liquid from its surface. This yields an overall mass balance.

$$\frac{d\Gamma}{dx} = -\dot{m}_{evp} \tag{7}$$

The evaporative mass flux is driven by a difference in temperature across the meniscus, the Clapeyron effect, and a difference in pressure across the meniscus, the Kelvin effect.

$$\dot{m}_{evp} = C\left(\frac{M_w}{2\pi RT}\right)^{1/2}\left\{\frac{P_v M_w h_{fg}}{RT_v T_i}\left(T_i - T_v\right) + \frac{V_l P_v}{RT_i}\left(P_l - P_v\right)\right\} \tag{8}$$

Finally, we tie the temperature difference across the liquid to the evaporative mass flux via:

$$T_i(x) - T_w = -\left(\frac{\dot{m}_{evp} h_{fg}}{k_l}\right) \tag{9}$$

Combining equations (5) – (9) allows us to express all the important features of the model in a single equation describing the film thickness profile of the meniscus. Equation (10) presents this in dimensionless form:

$$\frac{\partial}{\partial\xi}\left[\alpha\eta^3\frac{\partial^3\eta}{\partial\xi^3}-\alpha M\eta^3\frac{\partial}{\partial\xi}\left(\theta\frac{\partial^2\eta}{\partial\xi^2}\right)-\frac{3\beta}{\eta}\frac{\partial\eta}{\partial\xi}+\frac{3}{2}\varphi\alpha M\eta^2\frac{\partial\theta}{\partial\xi}\right]+$$

$$3\omega\frac{\partial}{\partial\xi}\left[\alpha\eta^2\frac{\partial^3\eta}{\partial\xi^3}-\alpha M\eta^2\frac{\partial}{\partial\xi}\left(\theta\frac{\partial^2\eta}{\partial\xi^2}\right)-\frac{3\beta}{\eta^2}\frac{\partial\eta}{\partial\xi}+\varphi\alpha M\eta\frac{\partial\theta}{\partial\xi}\right]=$$

$$-3Ca\sigma\left(\theta-\frac{\alpha}{\beta}\chi\frac{\partial^2\eta}{\partial\xi^2}-M\theta\frac{\alpha}{\beta}\chi\frac{\partial^2\eta}{\partial\xi^2}-\chi\eta^{-3}\right)$$

$$\text{Where, } \theta=\frac{\theta_0+\left(\frac{\alpha}{\beta}\chi\eta\frac{\partial^2\eta}{\partial\xi^2}+\chi n^{-2}\right)}{\theta_0+\eta+M\frac{\alpha}{\beta}\chi\eta\frac{\partial^2\eta}{\partial\xi^2}} \qquad (10)$$

Here:

$$\eta=\frac{h}{H}\qquad \xi=\frac{x}{L}\qquad \varphi=\frac{L^2}{H^2}$$

$$\alpha=\frac{\sigma H^4}{L^4}\qquad \beta=\frac{L^2}{A}\qquad \chi=\frac{\delta_0^3}{H^3} \qquad (11)$$

$$M=\frac{\gamma\Delta T_0}{\sigma_0}\qquad Ca=\frac{\nu_l\dot{m}_{id}}{\sigma_0}\qquad \omega=\frac{\beta_{slip}}{H}$$

The key length scales in the model are H, the film thickness in the thicker part of the meniscus at the edge of our experimental field of view, L, the extent of the meniscus corresponding to our field of view, and δ_0, the adsorbed film thickness. The scaling allows both η, the dimensionless film thickness and and ξ, the dimensionless position to span the range 0 – 1. The key dimensionless groups in the model are M, a measure of the fractional change in surface tension due to the temperature gradient, Ca, the capillary number measuring the relative strength of viscous to surface tension forces, and ω, a measure of the magnitude of the hydrodynamic slip length relative to the overall film thickness.

Equation (10) is a fourth order differential equation in terms of the film thickness subject to boundary conditions at the adsorbed film and bulk meniscus regions. Since we are able to measure both thickness and curvature via interferometry, the boundary conditions for the model were derived from the experimental measurements. Thus:

$$\xi=0\qquad \eta=\frac{\delta_o}{H}\qquad \frac{\partial^2\eta}{\partial\xi^2}=K_o \qquad (12)$$

$$\xi=1\qquad \eta=1\qquad \frac{\partial^2\eta}{\partial\xi^2}=K_1$$

4. RESULTS

The model was solved in COMSOL using a pair of general form PDE's. One tracked the film thickness and the other the film curvature. We believe this is the first time that a finite element formulation has been used to solve this type of problem and one of the few times that the problem has been solved as a boundary value problem. Most other solutions have been finite difference formulations or the equation has been decomposed into a series of four, first-order equations and solved via Runge-Kutta or other stiff integration routine.

Figures 6 and 7 show film thickness and curvature profiles for an octane meniscus as a function of the thickness of the adsorbed film, δ_0. Though there is not much apparent difference in the film thickness profiles, the effect shows up clearly in the curvature profiles. As the adsorbed film thickness increases, the effect of the intermolecular force interaction between solid-liquid-and

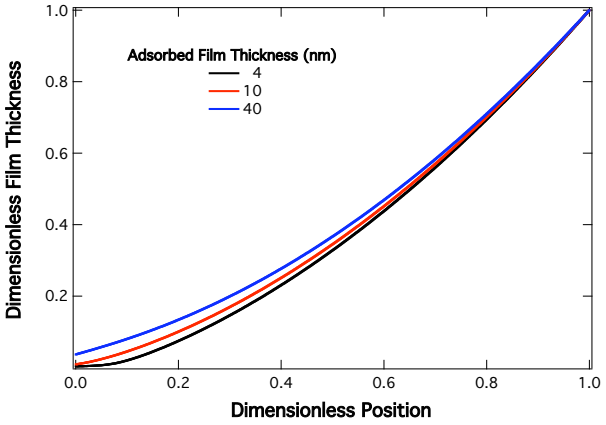

Figure 6 Simulated film thickness profiles for an evaporating octane meniscus as a function of the adsorbed film thickness, δ_0.

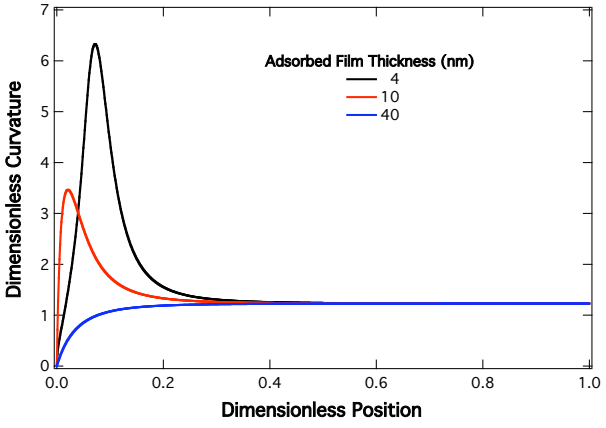

Figure 7 Simulated film curvature profiles for an evaporating octane meniscus as a function of the adsorbed film thickness, δ_0.

vapor decreases. This decrease leads to a sharp decrease in the curvature peak and hence the pressure drop required to push the required amount of fluid into

the active evaporation zone. We can use the changes observed in the predicted curvature profile to fit experimental data. Figures 8, 9, and 10 show fits to the curvature profiles for octane at two different power levels, 0.17 and 0.75 W, and for pentane. The experimental data indicates that hydrodynamic slip is required for the simulations to fit the data. Figure 8 shows what happens if slip is not included. Using the no-slip condition does not allow us to fit either the magnitude of the curvature peak or the location of the curvature peak. All three simulations show that the slip length required is on the order of 100 nm or so. This is in the general ballpark of hydrodynamic slip lengths reported by other investigators. Comparing the graphs for octane and pentane, one can see that as the peak curvature increases, the adsorbed film thickness must decrease. This agrees with what is observed experimentally as the power level is increased, though the exact value of the adsorbed film thickness used in the simulations does not agree with what was measured experimentally.

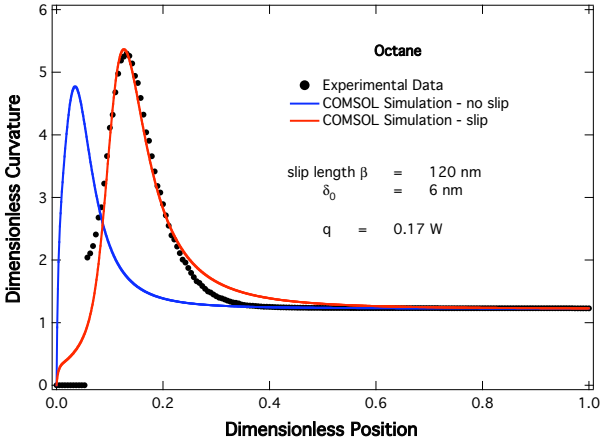

Figure 8 A comparison of experimental and simulated curvature profiles for an octane meniscus at a heat input of 0.17 W. Hydrodynamic slip is required to successfully fit the data.

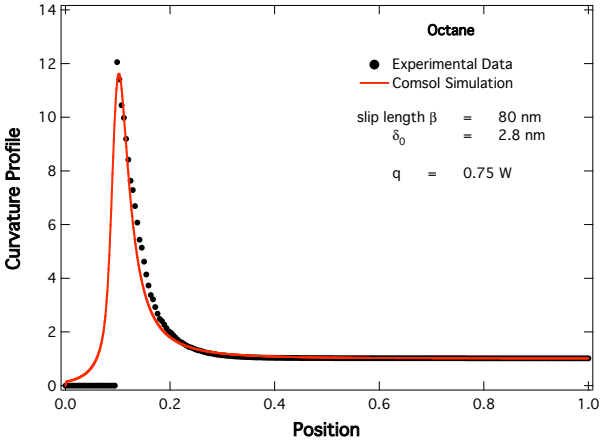

Figure 9 A comparison of experimental and simulated curvature profiles for an octane meniscus at a heat input of 0.75 W.

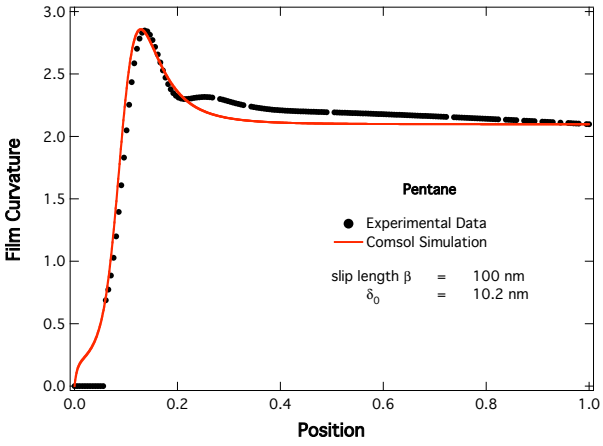

Figure 10 A comparison of experimental and simulated curvature profiles for a pentane meniscus.

Table 1
Adsorbed Film Thicknesses

Experiment	δ_0 Experimental	δ_0 Simulated
Octane 0.17 W	27.5	6
Octane 0.75 W	28.1	2.8
Pentane (0.075 W)	48.5	10.2

Table I shows the experimental and simulated adsorbed film thicknesses used in the model fits. Each graph shows the adsorbed film thickness used in the fitting. In general, the simulation required adsorbed film thicknesses that were about a factor of 5 lower than what was measured experimentally for the pentane and low power octane experiments and a factor of 10 lower than the high power octane experiment. The discrepancy between theory and experiment may arise from a number o sources. We have failed to include the effect of Marangoni stresses in the simulation. Such stresses occur due to the temperature gradients within the meniscus and the effect is greater, the higher the input power level. Adsorbed film thicknesses are difficult to resolve using our optical technique and experimental errors on the order of 50% are common. Ellipsometry would provide a more accurate measurement however it is difficult to get the required magnification necessary to obtain the measurement within the meniscus. Finally, we have used theoretical values for the Hamaker constant obtained using published dielectric properties of the liquid and solid substrate. Any minor contamination of the liquid or of the solid surface could lead to large changes in the value of the Hamaker constant, though perhaps not quite as large as what was needed for the simulations to match. Future work will aim to modify the model and obtain better agreement between the model parameters and the date. The fact that we obtain good fits to the data with realistic model parameters is very encouraging.

5. CONCLUSIONS

A model was developed to simulate the shape, the fluid flow, and the heat transfer occurring in extended menisci of octane and pentane. The model was based on the lubrication approximation and incorporated hydrodynamic slip at the liquid-solid interface. Good agreement was obtained between experiment an simulation showing the validity of the model formulation. This is the first time that a finite element scheme was used to solve the fourth-order evolution equation for the shape of an evaporating meniscus and one of the few times the model has been solved as a traditional boundary value problem.

6. ACKNOWLEGEMENTS

We acknowledge NASA under contract NNX09AL98G for support of this work.

7. NOMENCLATURE

A – Hamaker constant (J)
h – film thickness (m)
h_{fg} – heat of vaporization (J/kg)
k_l – thermal conductivity of the liquid (W/m K)
K – curvature (m^{-1})
L – length of field of view (m)
M_w – molecular weight (kg/kgmol)
$\dot{m}_{evp}$ – evaporation rate (kg/s)
P_l – pressure in the liquid (Pa)
P_v – pressure in the vapor (Pa)
q" – heat flux (W/m^2)
R – gas constant (J/mol•K)
T – temperature (K)
T_i – liquid–vapor interface temperature (K)
T_v – vapor temperature (K)
T_w – wall temperature (K)
U – velocity (m/s)
V_l – molar volume of liquid (m^3/mole)
x – distance along CVB axis (m)
y – distance from solid-liquid interface (m)

Greek symbols
β_{slip} – slip coefficient (m)
δ_0 – adsorbed film thickness (m)
γ – temperature coefficient of surface tension (N/mK)
Γ – mass flow rate per unit width (kg/m s)
μ – dynamic viscosity (kg/m s)
ν – kinematic viscosity (m^2/s)
Π – disjoining pressure (Pa)
ρ_l – liquid density (kg/m^3)
σ – surface tension (N/m)

8. REFERENCES

1. Horacek, B., et al., "Single nozzle spray cooling heat transfer mechanisms", *International Journal of Heat and Mass Transfer*, **48**, 1425-1438, (2005).
2. L. Zheng, J.L. Plawsky, P.C. Wayner Jr., and S. DasGupta, "Stability and oscillations in an evaporating corner meniscus," *Journal of Heat Transfer* **126**, 169, (2004).
3. M. B. Williams and S. H. Davis, "Nonlinear theory of film rupture," *J. Colloid Interface Sci.* **90**, 220 (1982).
4. C.C. Hwang, S. H. Chang, and J. L. Chen, "On the rupture process of thin liquid films," *J. Colloid Interface Sci.* **159**, 184 (1993).
5. E. Ruckenstein and R. K. Jain, "Spontaneous rupture of thin liquid films," *Chem. Soc. Faraday Trans.* **70**, 132 (1974).
6. A. Sharma and E. Ruckenstein, "An analytical nonlinear theory of thin film rupture and its application to wetting films," *J. Colloid Interface Sci.* **113**, 456 (1986).
7. J.P. Burelbach, S.G. Bankoff, and S.H. Davis, "Nonlinear stability of evaporating/condensing liquid films," *Journal of Fluid Mechanics* **195**, 463 (1988).
8. B. Reisfeld and S. G. Bankoff, "Nonlinear stability of a heated thin liquid film with variable viscosity," *Phys. Fluids A* **2**, 2066 (1990).
9. H. S. Kheshgi and L. E. Striven, "Dewetting: Nucleation and growth of dry regions," *Chem. Eng. Sci.* **46**, 519 (1991).
10. V.S. Ajaev, "Spreading of thin volatile liquid droplets on uniformly heated surfaces," *Journal of Fluid Mechanics* **528**, 279–296, (2005).
11. S.J. Gokhale, S. DasGupta, J.L. Plawsky, and P.C. Wayner Jr., "Reflectivity-based evaluation of the coalescence of two condensing drops and shape evolution of the coalesced drop," *Physical Review E* **70**, 51610, (2004).
12. S. Moosman, and G.M. Homsy, "Evaporating menisci of wetting fluids," *Journal of Colloid and Interface Science* **73**, 212–223, (1980).
13. D.M. Pratt, J.R. Brown, and K.P. Hallinan, "Thermocapillary effects on the stability of a heated, curved meniscus," *Journal of Heat Transfer* **120**, 220, (1998).
14. H. Wang, S.V. Garimella, and J.Y. Murthy, "Characteristics of an evaporating thin film in a microchannel," *International Journal of Heat and Mass Transfer* **50**, 3933–3942, (2007).